Uranium mineralization in the Alum Shale Formation (Sweden): Evolution of a U-rich marine black shale from sedimentation to metamorphism

Andreï Lecomte, Michel Cathelineau, Raymond Michels, Chantal Peiffert, Marc Brouand

Uranium mineralization in the Alum Shale Formation (Sweden): evolution of a U-rich marine black shale from sedimentation to metamorphism

Andreï Lecomte[1,*], Michel Cathelineau[1], Raymond Michels[1], Chantal Peiffert[1], Marc Brouand[2]

[1] GeoRessources, Université de Lorraine, CNRS, CREGU, Boulevard des Aiguillettes B.P. 70239 F-54506 Vandoeuvre lès Nancy, France

[2] AREVA, 1 place Jean Millier. F-92084 Paris La Défense Cedex, France

*Corresponding author: GeoRessources, Boulevard des Aiguillettes B.P. 70239 F-54506 Vandoeuvre-lès-Nancy, France

E-mail address: Andrei.Lecomte@univ-lorraine.fr

Tel: (33) (0)3 83 68 47 29

Fax: (33) (0)3 83 68 47 01

Graphical abstract

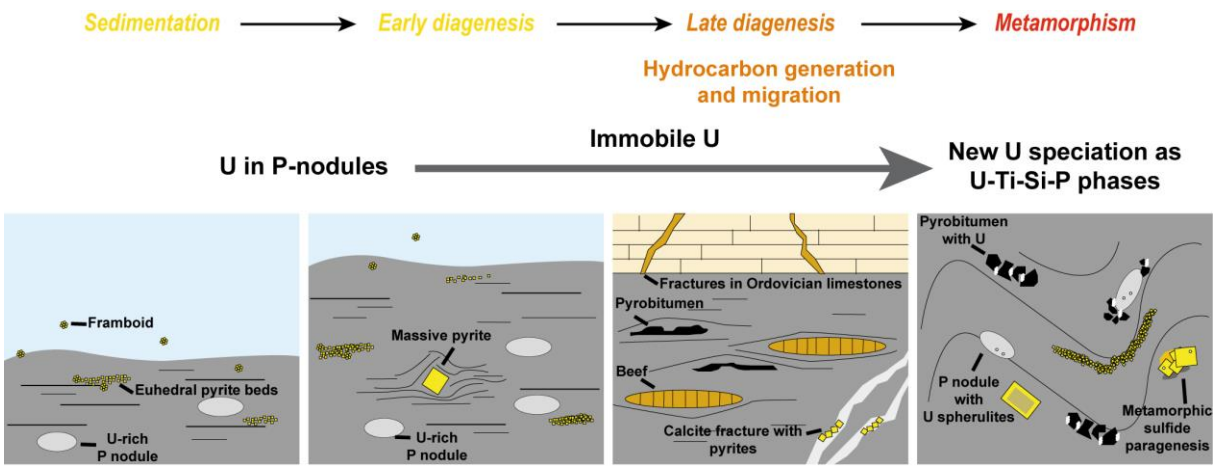

Abstract

The Alum Shale Formation is a metal-rich black shale, deposited on the Baltoscandian platform between Middle Cambrian and Early Ordovician. These black shales may be of particular economic interest for their relatively high uranium content (100-300 ppm) and their wide distribution from Norway to Estonia. Scandinavian Alum Shale may thus constitute a great potential resource of uranium, as a low grade ore. The Alum Shale Formation is particularly interesting to study the mineralogical expression and content of uranium in series submitted to progressive burial and metamorphism. For this purpose, the behavior of U, P, Ti and organic matter was studied on a series of representative samples from most Alum Shale prospection zones. In southern Sweden, where Alum Shale underwent fairly shallow burial, uranium concentrations have no mineralogical expression except a rather high U content of biogenic phosphates. Calcite concretions (beefs) and fractures recorded the migration of hot overpressured hydrocarbons and brines from thermally mature areas to immature Alum Shale. However, thermal maturation and fluid migration did not allow remobilization of uranium and metals. At the opposite, in northern Sweden, where the series were folded, duplicated and submitted to low grade Greenschist metamorphism during Caledonian orogeny, phospho-silicates U-Si-Ca-P (±Ti ±Zr ±Y) and minor amounts of uraninite are identified and indicate that U, P, and Ti were mobile and precipitated as new phases. The effect of metamorphism is therefore important to consider as the leachability of U, especially during (bio)-hydrometallurgical processes, which will be by far different between the two considered areas.

45 Keywords: uranium; Alum Shale; organic matter; metamorphism; fluid inclusions;
46 hydrocarbons

47

1. Introduction

Lower Palaeozoic black shales extend over most of northern Europe, from Norway to Estonia across the Baltic Sea. These sediments were deposited on the Baltoscandian platform during an interval of great tectonic stability (Andersson *et al.*, 1985). In particular, the Alum Shale Formation is an organic-rich marine sequence deposited over present Scandinavia between Middle Cambrian and Early Ordovician. The name Alum refers to the alum salt $KAl(SO_4)_2 \cdot 12H_2O$ that formed under supergene conditions and was extracted from this black shale over 300 years ago. As many other black shales deposited in marine environments, Alum Shale contains high metal concentration compared to ordinary shales, especially Ni, Mo, Co, Cu, Zn, U, V, As, Se, Ag, Au and PGE (Vine and Tourtelot, 1970; Holland, 1979; Wignall, 1994). Nevertheless, Scandinavian Alum Shale is of particular interest because of its somewhat higher uranium content (100-300 ppm) and its wide extension. Therefore, they may constitute a potential uranium resource for the future.

The Alum Shale Formation is particularly interesting for the study of the mineralogical expression and content of uranium in series submitted to progressive burial and metamorphism. In order to understand the behavior of U, P, Ti and organic matter at increasing P-T conditions, a series of representative samples from most Alum Shale prospection zones were studied: i) samples from southern Sweden, where Alum Shale underwent rather shallow burial, and ii) samples from northern Sweden, where Alum Shale was folded, duplicated and submitted to low grade Greenschist metamorphism during Caledonian orogeny. The main objective was to identify the mineralogical expression of metals and uranium in these low grade ores,

and especially changes expected to occur during burial and metamorphism. Indeed, the nature of the U bearers is poorly known, and was almost not studied, most available data dealing with bulk U grades for evaluation of the mining potential and radioprotection purposes (Armands, 1972; Parnell, 1984; Andersson *et al.*, 1985; Buchardt *et al.*, 1997). Knowledge about the form at which U occurs in the ore is valuable information regarding ore treatment processes and recoverable reserve estimation.

2. Geological setting

In Sweden, the Alum Shale Formation can be subdivided into three geographical and structural provinces (Fig. 1): (a) autochthonous platform cover units (southern Sweden) lying on the Proterozoic basement, unaffected by Caledonian orogeny; (b) parallochthonous Alum Shale duplicated along the Caledonian Front with a metamorphic and hydrothermal imprint during the Caledonian orogeny (420-400 Ma); (c) allochthonous units in Sweden and Norway showing Greenschist facies metamorphic grade (Sundblad and Gee, 1984). The Alum Shale Formation is a marine sequence deposited between Middle Cambrian and Early Ordovician (Tremadoc) on Lower Cambrian sediments, the latter resting on a crystalline Palaeoproterozoic basement (Nielsen and Schovsbo, 2007). The sedimentation took place in a shallow-water epicontinental basin bordered by the Tornquist Sea to the South and the Iapetus Ocean to the North and West (Scotese and McKerrow, 1990). In the Early Cambrian, rising sea-level led to extensive flooding over the Baltoscandian sector of Baltica. A succession of transgressive and regressive

events occurred early to Middle Cambrian and ended with major Hawke Bay regression, terminating deposition of Lower Cambrian sediments (Nielsen and Schovsbo, 2011). During Middle Cambrian, marine transgression shifted the paleo-shoreline to the north-east (Andersson *et al.,* 1985; Buchardt *et al.,* 1997; Schovsbo, 2002). From then, Baltoscandian epicontinental sea was characterized by extremely low depositional rates and dysoxic to anoxic conditions, especially in the deeper parts of the basin (Nielsen and Schovsbo, 2015). These particular conditions prevailed until Early Ordovician and favored Alum Shale deposition. During Caledonian orogeny, Alum Shale underwent Greenschist facies metamorphism. Besides, in the Caledonian foreland basin and in southern Sweden and Denmark, deep burial (up to 4 km) initiated thermal maturation of organic matter and hydrocarbon generation (Buchardt *et al.*, 1997, Schovsbo *et al.*, 2011).

The Alum Shale Formation is generally 15-35 meters thick but extremely variable, from 2 meters in Öland to 95 meters in Skåne. In the Caledonides, the formation is duplicated by thrust sheets and the thickness reaches up to 180 meters (Andersson *et al.*, 1985). Scandinavian Alum Shale is dominated by organic-rich (up to 20% TOC) marine black shales, with variable proportions of grey shales and silt beds, limestones and carbonate concretions. The latter generally trapped large amounts of hydrocarbons (Andersson, 1985; Thickpenny, 1984). In the Upper Cambrian, small lenses of organic matter (kolm) occur and are often highly uraniferous (up to 5000 ppm).

3. Sampling and analytical procedure

Sampling procedure aimed at selecting representative black shale samples of various thermal maturity, from immature or slightly mature Alum Shale to metamorphic rocks. Several locations were selected, with the least mature black shales (Västergötland, Östergötland, Närke and Öland), overmature Alum Shale in Skåne and metamorphic Alum Shale (Lövstrand, Myrviken and Tåsjö). Sampling locations are indicated on figure 1. Samples were taken on several drill cores stored in SGU's coreyards (Geological Survey of Sweden) and are listed in table 1. Most of these cores correspond to historical drilling projects. Studies were conducted on thin sections and polished sections, the latter included with Araldite in an aluminum ring of 25 mm diameter.

Petrographical studies were done using optical microscopes in reflected light, a SEM Hitachi S-4800 coupled to a ThermoNORAN Si(Li) detector, and a FEG SEM JEOL 7600F (hot cathode) with an Oxford Instruments SDD-type EDS spectrometer. Analyses were performed at 10 kV. Electron Probe Micro-Analysis (EPMA) analyses were performed using a CAMECA SX100, with an acceleration voltage of 20 kV and beam current of 20 nA.

X-Ray diffractograms were acquired using a D8 Bruker diffractometer with a non-monochromatic CoKα radiation (35 kV, 45 mA). Air-dried (AD), ethylene glycol (EG)-saturated and 550°C-heated XRD preparations (fractions < 2 µm) are analyzed to determine diffracted intensities of clays over 3-40°2θ range with a 0.02°2θ step and 3 seconds per step.

Multi-elements concentrations in phosphate nodules, carbonaceous residues and fluid inclusions were measured using a LA-ICP-MS system composed of a

GeoLas excimer laser (ArF, 193 nm, Microlas, Göttingen, Germany) associated with an Agilent 7500c quadrupole ICP-MS. Quantification of the results was achieved using the standard NIST SRM 610 (Pearce *et al.*, 1997) and subroutine data processing (Leisen, 2011). Sample density was calculated for several metamorphic and immature Alum Shale, measuring their volume by water immersion after paraffin coating.

Raman spectra of carbonaceous material from the Alum Shale were acquired using a LabRAM HR microspectrometer (Horiba Jobin Yvon) equipped with a 600 gr/mm grating, using the 514.53 nm radiation of an Ar^+ laser with a final power of about 1mW (Stabilite 2017, Newport Spectra Physics). The laser was focused in the sample using a 100X objective. Acquisition time was set in such a way that the intensity reached at least 1/3 of the saturation level of the CCD (i.e. 20000 counts per second). Each measurement is the sum of 6 spectrum acquisition of 30 to 40 seconds each.

Sulfur isotope compositions were measured with a Cameca IMS1280 HR2 (CRPG, Nancy, France) using simultaneous measurements of ^{32}S, ^{33}S, and ^{34}S in multicollection mode, with a Cs^+ primary beam of 1nA intensity. Data were corrected for instrumental mass fractionation using several sulfide standards: Maine (pyrite, $\delta^{34}S$ = -19.3‰), Spain (pyrite, $\delta^{34}S$ = -2.95‰), NiS ($\delta^{34}S$ = 19.14‰). Analyses consisted of 3 minutes of presputtering followed by data acquisition in 40 cycles of 3 seconds. Sulfur isotope measurements are reported as part per thousand deviations with respect to Canyon Diablo Troilite using δ notation.

Microthermometric data were acquired on a Linkam MDS 600 stage coupled with an Olympus BX-51 microscope equipped with a UV-light source (Mercury

lamp, λ=365 nm) allowing the recognition of fluorescent petroleum-bearing fluid inclusions. Phase transition temperatures can be measured between -196°C and 600°C, with an accuracy of ±0.1°C. In this study we measured homogenization temperature of hydrocarbon-bearing and aqueous inclusions, which correspond to the transition between a biphasic liquid–vapor inclusion and a monophasic liquid or gas inclusion.

Raman analyses of aqueous inclusions were performed using a LabRAM HR microspectrometer (Horiba Jobin Yvon), using the 457 nm radiation of an Ar^+ laser with a final power of about 80 mW. Each measurement is the sum of 4 spectrum acquisition of 30 to 60 seconds each. Beam parameters and accumulation time were adjusted to obtain the best signal/background ratio. Chlorinities of aqueous phases were calculated using the method of Dubessy *et al.* (2002).

Infrared spectra of hydrocarbons in inclusions are recorded in transmission mode using a Bruker Vertex 70 Fourier transform infrared spectrometer coupled to a Hyperion 3000 microscope. The microscope is equipped with a MCT (mercury cadmium telluride) cooled at 77 K. The size of the beam can be reduced down to a diameter of 20µm with X15 objective magnification. The IR spectra are obtained in the mid-infrared region with a 2 cm^{-1} spectral resolution. Each sample is scanned about 90 seconds and the influence of atmospheric water and carbon dioxide was always subtracted.

Confocal laser scanning microscopy (CLSM) measurements were acquired on a Biorad rainbow system coupled to a Nikon inverted microscope following procedure described in Pironon *et al.* (1998). 3D reconstruction was used to calculate the volume

of gaseous filling at room temperature. Isochores and isopleths of hydrocarbon-bearing inclusions were determined with FIT-Oil software (Fluid Inclusion Thermodynamic-Oil, evolution of PIT software; Thiéry *et al.*, 2000) using homogenization temperature and previously calculated α/β parameters. α/β parameters represent the composition of heavy alkanes (≥ C10) and light alkanes , respectively (Montel, 1993; Thiéry *et al.*, 2000). Isochores of aqueous inclusions in the CH_4-H_2O-NaCl system, with various NaCl concentration and CH_4 concentration below 1 molal, were calculated using the method of Zhang and Frantz (1987).

4. Results

4.1. Mineralogy of the Alum Shale Formation

The Alum Shale Formation is an organic-rich marine black shale showing variable facies, from dark gray calcareous mudstone to black laminated mudstone depending on the organic matter content (Fig. 2). Sulfides, especially pyrites, are disseminated throughout the shale. Metamorphic Alum Shale is often folded and present calcite precipitation as pressure shadows around massive pyrite or inside fractures with pyrobitumen. The detrital fraction is composed of quartz, feldspars (orthose and albite) and clays (Fig. 3). Clays composition is slightly variable but always remains dominated by illite and illite-smectite mixed-layer minerals. The latter are characterized by a left shoulder on illite main peak and doublets on secondary peaks. Smectite is emphasized by peak shift after glycolation and peak disappearance after heating at 550°C. Minor kaolinite and chlorite are also observed. With deep burial and metamorphism, illite peak gets thinner and shows the illite-muscovite transition.

209

210 **4.2. Geochemistry of the Alum Shale Formation**

211 As many other black shales deposited in marine environments, Alum Shale
212 contains metal concentration higher than ordinary marine shales. In figure 4, whole-
213 rock concentrations of several elements (As, Co, Cu, Cr, Mo, Ni, Pb, Th, U, V, Zn) in
214 the Alum Shale Formation and reference metalliferous black shales are plotted and
215 compared to the "Marine Shales" (Turekian and Wedepohl, 1961). Metalliferous
216 black shales include Chinese Cambrian black shales from Tarim basin (Yu *et al.*,
217 2009), Ronneburg Silurian black shales (Lippmaa *et al.*, 2011) and American Devonian
218 black shales (Ohio shale, Lewis *et al.*, 2010). Complete dataset is in table 2 for eight
219 metamorphic samples (Myrviken, Lövstrand and Tåsjö) and thirteen non
220 metamorphic samples (Närke, Östergötland, Öland, Skåne and Västergötland). The
221 Alum Shale Formation is remarkable because of a particularly higher uranium
222 content compared to other metalliferous black shales. In Upper Cambrian Alum
223 Shale, U content is generally higher than 100 ppm (mean 118±48 ppm) and may reach
224 several hundreds ppm. On the contrary in most metalliferous black shale worldwide,
225 U content does not exceed a few tens of ppm.

226 Besides, in Scandinavian Alum Shale, organic carbon content and total sulfur
227 content (TS) are generally high but values are scattered. Total Organic Carbon (TOC)
228 ranges between 5 and 20 wt.% (mean 12±4 wt.%) and total sulfur between 4.6 and 6.3
229 wt.% (mean 5.5±0.6 wt.%). When plotted in a TS vs TOC diagram (Fig. 5a), Alum
230 Shale analyses display a positive correlation across "euxinic sediments" and "normal
231 oxygenated sediments" fields. This correlation line crosscut TS-axis at around 4.9
232 wt.%. Moreover, whole-rock V/Cr and V/(V+Ni) ratios are high, between 4.26 and

18.67 (mean 9.19±4.65) and between 0.68 and 0.85 (mean 0.77±0.04), respectively (Fig. 5b).

Finally, when plotted against both organic carbon (Fig. 6a) and phosphorus (Fig. 6b) concentrations, uranium content displays a positive correlation. In particular, density-corrected uranium concentration increases along with total organic carbon following two different trends for metamorphic and immature samples. Indeed, in metamorphic Alum Shale, U concentration increases with a steeper slope than in immature samples. Thus, for equivalent percentages of organic carbon, metamorphic samples are twice as rich as immature samples.

4.3. Carbon, sulfur and uranium in immature Alum Shale

4.3.1. Organic matter accumulation

In immature Alum Shale, organic matter is composed of fluorescent liptinite and non-fluorescent pseudo-vitrinite (Fig. 7a and 7b). In most immature samples, liptinite displays yellow-green fluorescence, whereas Västergötland's lipnite is scarcer and shows orange-brown fluorescence. Rock-Eval results are listed in table 3. Rock-Eval S1 values are between 0.45 and 1.71 mg HC/g Rock and S2 values between 13.00 and 99.94 mg HC/g Rock. Hydrogen Index (HI) values range between 132 and 544 mg HC/g TOC. Tmax values range between 406 and 426°C confirming immature organic matter (Tissot and Welte, 1984). When plotted in a S2 versus TOC diagram (Fig. 8), immature Alum Shale lines up on the Type II organic matter trend (Langford and Blanc-Valleron, 1990). Västergötland's Alum Shale appears to be anomalous with lower IH values, which may be related to previously described maceral composition. In IH-Tmax (Fig. 9) and S1-S2 (Fig. 10) diagrams, organic

matter falls in the immature Type II area, with an excellent petroleum potential.

4.3.2. Sulfide paragenesis during sedimentation and diagenesis

The Alum Shale Formation contains sulfide mineralization, in particular pyrites with various shapes and distributions (Fig. 11): (a) disseminated spherolites or framboids in shale layers and rarely in bitumen; (b) small anhedral crystals scattered in black shale; (c) beds or clusters of small euhedral crystals, mostly underlining sedimentary bedding; (d) massive anhedral to euhedral pyrites; (e) pyrite cements and overgrowths in fractures.

In immature Alum Shale, five pyrite generations (named Py1 to Py5 in tables and figures) have been identified over petrographic features. The first generation corresponds to disseminated framboids and small euhedral crystals following shale stratification. The second generation occurs as beds or nodules of massive pyrite and may be locally reworked and cemented framboids clusters. This recrystallization stage seems to be synchronous with partial pyrite cementation of detrital grains. The third generation is represented by large pyrite crystals which are either scattered in the shale or grow on recrystallized -mainly framboids- beds perpendicularly to the shale bedding. Massive pyrites display a homogeneous texture, sometimes with growth zones, and may deform shale lamination. The fourth generation corresponds to fracture infillings as pyrite cement or large-scale euhedral crystals. Cementation is not homogeneous and has high porosity. The fifth generation occurs as homogeneous pyrite veins and small pyrite overgrowths.

Trace elements content in sulfides is often helpful to distinguish different precipitation conditions. In the case of immature Alum Shale, no particular

enrichment was measured in pyrites, except for framboids, where Cu and As concentrations are higher than co-genetic euhedral pyrites (Fig. 12a and b).

Every pyrite generation was analyzed by SIMS (Secondary Ion Mass Spectrometry) to determine sulfides isotopic composition. Sulfur isotopic data are listed in table 4 and represented as a histogram (Fig. 13). First generation (clusters of framboids and euhedral crystals) shows high $\delta^{34}S$ values between 30 and 40‰. One single framboid was analyzed and has a slightly negative $\delta^{34}S$ (-4‰). Second pyrite generation values range between 22 and 26‰. Third generation correspond to massive pyrites. Analyses yield $\delta^{34}S$ results between 18 and 25‰. Inside most crystals, neither chemical zoning nor isotopic composition gradient was observed. However, isotopic zoning was measured into a large pyrite with $\delta^{34}S$ increasing from core to rim (16‰ to 23‰). Besides, a small pyrite inclusion in the center shows high sulfur isotopic composition ($\delta^{34}S$ = 33‰) similar to that of first generation. Fourth generation cementing massive pyrites shows homogeneous $\delta^{34}S$ values (30-31‰). Rare subhedral pyrites on the edges of these cemented areas have the same isotopic signature. In homogeneous fracture infillings and late pyrite overgrowths (fifth generation), $\delta^{34}S$ ranges between 19 and 23‰.

4.3.3. Uranium concentration in immature shales

No detectable uranium mineral was observed in immature Alum Shale. However, in the Alum Shale Formation, calcium phosphate nodules are disseminated and generally parallel to the stratification. These nodules are several hundreds of micrometers long and are composed of apatite-(CaF[OH]) (Fig. 14). REE analyses (Table 5) were carried out using LA-ICP-MS. REE spectra normalized to

North American Shale Composite (NASC REE concentrations after Gromet *et al.*, 1984) are plotted in figure 15a. Apatite-(CaF[OH]) nodules display bell-shaped REE patterns, centered on Eu. Such patterns are similar to those measured on pre-jurassic biogenic marine phosphates. Uranium concentration in these phosphate nodules were measured with LA-ICP-MS. The results (Table 5) show between 131 and 185 ppm uranium grades.

4.4. Impact of burial and thermal maturation on organic matter and uranium

4.4.1. Thermal maturation of the Alum Shale Formation and oil generation

Burial and thermal maturation of Alum Shale lead to oil and gas generation. Hydrocarbons are present as pyrobitumen or impregnation of phosphate nodules in the black shale, but also as fluid inclusions in calcite crystals (Fig. 16a and b), which occur as: (a) carbonate concretions composed of large fibrous calcite crystals, up to 10 centimeters long. These concretions, parallel to shale bedding, may be up to 1.5 meters long and 50 centimeters thick. The core is made of microcrystalline calcite and bioclasts, whereas rims are recrystallized in pure calcite with frequent cone-in-cone structures. (b) brecciated levels composed of centimetric non-oriented angular particles of pure calcite in a matrix of microcrystalline calcite and detrital grains; (c) fractures with calcite infillings in Ordovician limestones.

Fluid inclusions (Fig. 16c to d), in particular petroleum inclusions, are abundant in breccias and fractures, but scarce in fibrous crystals. They are mostly biphasic L_w-V (liquid water and vapor bubble) or L_{oil}-V (liquid oil and vapor bubble), although some monophasic L_{oil} or triphasic L_w-L_{oil}-V inclusions have been observed. In 3-phase inclusions, oil always occurs as droplets in aqueous phase and vapor

phase is contained in oil (Fig. 16f). Shapes vary from rounded or ellipsoidal shapes for aqueous or small oil inclusions to irregular shapes for large petroleum inclusions. Most inclusions are small (<10 μm) although a few can reach several tens of microns. Distribution of fluid inclusion is not homogeneous in calcite crystals. They are generally clustered (several inclusions to tens of inclusions of various size) or distributed along calcite cleavage planes. These fluid inclusion planes are tens to hundreds of microns long and are always constrained within a single crystal. Oil is generally yellow to brown, rarely colorless. Under UV-epifluorescence, petroleum inclusions display various colors: yellow to orange-brown for most of them, white, blue, or green-blue. Isolated and clustered inclusions in concretions or fractures are considered as primary inclusions trapped during calcite growth. Short intragranular fluid inclusion planes are taken as primary when parallel to cleavage or rarely pseudo-secondary when randomly oriented. A few planes are obviously posterior to calcite crystallization and are labeled as secondary. These intergranular trails contain small oil inclusions with blue-colored UV-epifluorescence and crosscut crystal fabrics.

Homogenization temperatures (T_h) were measured on 213 fluid inclusions (185 oil inclusions and 28 aqueous inclusions) from 6 concretion samples, and 207 inclusions (172 oil inclusions and 35 aqueous inclusions) in 3 limestone fractures. Distinction between inclusions was made according to the parameters previously described: host rock (concretion/breccia or fractures), timing of formation (primary, pseudo-secondary or secondary), liquid phase (oil or water) and fluorescence color (yellow-orange-brown or white-blue). Microthermometry results are presented in

352 histograms (Fig. 17).

353 In calcite crystals from concretions and breccias (Fig. 17a), homogenization
354 temperatures show a wide range of values between 60 and 200°C. T_h distribution of
355 petroleum inclusions is bimodal with a primary mode between 70 and 100°C and a
356 secondary mode between 120 and 150°C. Inclusions with yellow-orange-brown
357 fluorescence have principal and secondary modes centered around 80°C and 130°C,
358 respectively. Inclusions with white-blue fluorescence have principal and secondary
359 mode centered around 90°C and 140°C, respectively. T_h of aqueous inclusions range
360 between 90 and 170°C, with a unimodal distribution centered around 140°C. The
361 distribution of oil inclusions is essentially driven by primary and pseudo-secondary
362 inclusions. T_h of blue-fluorescing secondary inclusions range between 83 and 105°C.
363 In fractures (Fig. 17b), inclusions have a wide range of T_h between 5 and 190°C.
364 Inclusions with yellow-orange-brown fluorescence have principal and secondary
365 modes centered around 100°C and 150°C, respectively. Inclusions with white-blue
366 fluorescence have unique mode centered on 100°C. T_h of aqueous inclusions range
367 between 90 and 180°C, with a unimodal distribution centered around 150°C.

368 Determination of chlorinity in aqueous phase and gas content in fluid
369 inclusions were performed with Raman spectroscopy. Only aqueous inclusions were
370 analyzed due to high fluorescence of hydrocarbons disrupting Raman signal. Water
371 chlorinity was calculated at room temperature from band area ratio of water phase. 9
372 inclusions in concretions have salinities between 9.5 and 20.9 wt.% eq. NaCl (mean
373 15±3.2 wt.% eq. NaCl). 3 inclusions in fractures have salinities between 12 and
374 19.4 wt.% eq. NaCl (mean 16±3.7 wt.% eq. NaCl). Besides, composition of gaseous

375 phase was analyzed in aqueous inclusions. Methane is always detected and is
376 sometimes associated with carbon dioxide. However, dissolved methane
377 concentration at homogenization temperature was not detected, which indicates
378 rather low concentration in CH_4.

379 Infrared spectroscopy was used to investigate composition of petroleum
380 inclusions (Table 6 for inclusions observed with confocal laser scanning microscopy).
381 CH_4 content in concretions and fractures is variable and range between 26.2 and
382 47.3 mol% (mean 38.3±7.8 mol%) and between 16.9 and 48.7 mol% (mean
383 30.9±9.8 mol%), respectively. CO_2 was not detected in most concretion inclusions but
384 was present at low concentration (0.3 to 2.9 mol%) in fracture inclusions. In the same
385 way, alkane content varies greatly within samples: 52.5 to 73.8 mol% (mean
386 61.7±6.9 mol%) in breccias and concretions; 50.7 to 80.9 mol% (mean 68±9.5 mol%) in
387 limestone fractures. All these parameters are not correlated with host mineral,
388 homogenization temperature or fluorescence color. Only CO_2 concentration seems to
389 be slightly higher in fractures than in concretions. On the contrary, CH_2/CH_3 ratio is
390 clearly distinct between host minerals. In concretions and breccias, ratios vary
391 between 1 and 3.6 (mean 2.4±0.9, a single inclusion has a ratio close to 1) whereas in
392 fractures ratios vary between 0.6 and 1.6 (mean 1.1±0.4). In concretions, higher
393 CH_2/CH_3 ratios imply longer aliphatic chains and therefore lower maturity than in
394 fractures. Besides, a correlation is observed between CH_2/CH_3 ratios related to oil
395 maturity and fluorescence color: inclusions with a ratio close to 1 show white-blue
396 fluorescence, yellow fluorescence around 2 and orange-brown fluorescence above
397 2.5. In fractures, predominance of inclusions with with-blue fluorescence over rare

398 inclusions with orange-brown fluorescence may indicate greater maturity of oil
399 trapped in fractures, as already suggested by CH_2/CH_3 ratios.

400 Confocal laser scanning microscopy was performed on several petroleum
401 inclusions (features in table 6) to measure oil volume whereas volume of the gas
402 bubble is determined by spherical approximation. Degree of gaseous filling (F_v) is
403 used with microthermometry results and thermodynamic modeling to estimate
404 pressure-temperature trapping conditions of petroleum inclusions. F_v ranges
405 between 3 and 27% for inclusions in concretions and between 5 and 25% for
406 inclusions in fractures. F_v vs T_h diagram (Fig. 18) is useful to characterize petroleum
407 composition from black oil to dry gas. Oil trapped in concretions falls in the range of
408 heavy black oils and appears to be heavier than oil in fractures, which ranges
409 between black oil and light oil.

410 Thermodynamic properties and P-T trapping conditions of fluids can be
411 reconstructed with thermometric and compositional data of petroleum and aqueous
412 inclusions. Petroleum isopleths and isochores are represented in figure 19. No
413 aqueous inclusion was observed in the immediate vicinity of modeled oil inclusions.
414 Therefore, aqueous isochores were calculated with contemporaneous inclusion from
415 the same sample and are represented by a band rather than lines. Dashed lines
416 correspond to a "standard" isochore calculated using the mode of T_h distribution and
417 average salinity. P-T trapping conditions are determined by the intersection of oil
418 and aqueous isochores. In concretions, primary mode hydrocarbon inclusions
419 (Th<100°C) indicate trapping temperature between 170 and 190°C and trapping
420 pressure between 650 and 750 bars. With secondary mode inclusions (T_h>110°C),

trapping temperature and pressures range between 150 and 170°C and 180 and 280 bars, respectively. In fractures, P-T domains appear to be much more continuous from high pressure to relatively low pressure. Low T_h inclusions indicate trapping temperature around 180-190°C and pressures between 500 and 600 bars. Most oil inclusions with T_h above 100°C correspond to trapping temperature around 170-180°C and trapping pressure between 350 and 430 bars.

Finally, LA-ICPMS analysis of fluid inclusions trapped in calcite did not show any significant concentration in metal or uranium (detection limit of 0.5 to 1 ppm).

4.4.2. Impact of burial diagenesis on uranium content: experimental input

The TOC richest immature sample (from Närke), was heated in gold cells during 24 hours at 350°C and 700 bars to simulate thermal maturation and hydrocarbon generation. Pyrolyzed matter was then solvent-extracted. Hydrocarbon extracts and pyrolysis residues were both analyzed and uranium content measured. LA-ICPMS analysis did not allow us to detect any particular uranium content in the solvent extracts (within detection limit). However, residues contain similar, but slightly higher, uranium concentrations, compared to unheated shale (139.9 and 132.4 ppm versus 124.5 ppm). TOC values decreased by more than 20% with hydrocarbon generation, from 18.48 wt.% to 14.41 and 14.24 wt.%. Density-corrected values are plotted in figure 6a. Alum Shale samples display a U-constant evolution during thermal maturation.

4.5. Impact of metamorphism on carbon, sulfur and uranium mineralization

4.5.1. Organic matter behavior with metamorphism: geothermometer

445 ***application***

446 The Raman spectrum of carbonaceous matter is composed of several peaks
447 situated in first order (1100–1800 cm^{-1}) and second-order (2500–3100 cm^{-1}) regions
448 (Tuinstra and Koenig, 1970; Nemanich and Solin, 1979). The number, position, width
449 and intensity of peaks depend on the degree of structural organization of
450 carbonaceous material, from very disordered carbonaceous matter to graphite and it
451 can be used as a geothermometer (e.g. Beyssac *et al.*, 2002, 2003(a), 2003(b); Beyssac
452 and Lazzeri, 2012; Lahfid *et al.*, 2010).

453 In metamorphic Alum Shale samples, organic matter is composed of
454 disseminated pseudo-vitrinite particles and bitumen veinlets in the schist. Bitumen
455 with conchoidal fractures can also be found in veins, trapped in calcite (Fig. 7c to f).
456 Raman spectroscopy of carbonaceous material (RSCM) was applied on different
457 metamorphic samples from the Caledonian front (Tåsjö and Myrviken), in order to
458 characterize the degree of organization of organic matter and estimate metamorphic
459 temperature. Both pseudo-vitrinite and bitumen have been studied and Raman data
460 are provided in table 7. Organic material in the Alum Shale shows first-order and
461 second-order regions corresponding to very disordered carbonaceous matter (Fig.
462 20a). We thus applied a fitting procedure using five bands with Lorentzian profiles
463 (Lahfid *et al.,* 2010; Lecomte *et al.,* 2014). The decomposed first-order region of
464 carbonaceous matter spectrum (Fig. 20b) is composed of a predominant graphite
465 peak including a graphite band s.s. (G) at 1595±3 cm^{-1} and a defect band (D2) at
466 1608±3 cm^{-1}, and a secondary composite (D) peak with major defect band (D1) at
467 1332±2 cm^{-1} and a left shoulder (defect band (D4) at 1218±9 cm^{-1}). In disordered CM,
468 intensity of the valley between (D1) and (G) is high and indicates the existence of

another band (D3) at 1513±8 cm^{-1}.

Following procedure described by Lahfid *et al.* (2010), using two area ratios RA1 = (D1 + D4) / (D1 + D2 + D3 + D4 + G) and RA2 = (D1 + D4) / (D2 + D3 + G), yield an estimate of the maximal temperature that underwent the organic matter: RA1 = 0.0008T + 0.3758 and RA2 = 0.0045T + 0.27 (Table 7). In metamorphic Alum Shale, calculated temperatures are slightly higher at Tåsjö (305±11°C with RA1 and 302±14°C with RA2) than at Myrviken (285±11°C with RA1 and 279±13°C with RA2). In such low-grade metamorphic systems, temperature is considered to be the key parameter for carbonaceous matter evolution at geological time scales even if other parameters (pressure, time or deformation) are less well constrained (Beyssac *et al.*, 2003(a); Lahfid *et al.*, 2010).

4.5.2. Modification of sulfide paragenesis

In metamorphic Alum Shale from the Caledonian front, all pyrites generations described in immature shales (Py1 to Py5) have been affected by metamorphism during Caledonian orogeny. Several particular modifications can be identified, namely: (a) intense fracturing throughout the Alum Shale, with pyrite and calcite fillings, and numerous pyrite overgrowths (Fig. 21a and b). In particular, these overgrowths are much more frequent in metamorphic samples than in immature ones, and occur not only in fractures but also around previous pyrite generations, often completely cataclased by deformation. These secondary crystals can reach several tens of microns and calcite precipitates in pressure shadows around massive pyrites; (b) plastic deformation of pyrite beds (framboids and small euhedral crystals), initially parallel to stratification (Fig. 21c); (c) pressure-solution features on

493 small euhedral pyrites, with interpenetrating grain boundaries (Fig. 21d); (d)
494 precipitation of new sulfides (chalcopyrite and sphalerite) coexisting with late pyrite
495 after fracturing stage. Chalcopyrite and sphalerite generally occurs as cements
496 around euhedral pyrites or as fracture fillings (Fig. 21e to h).

497 In metamorphic Alum Shale, the latest pyrite generation (named Py6), which
498 is sub-synchronous with chalcopyrite and sphalerite, is enriched in Ni, As, Se and Cd
499 compared to synsedimentary pyrites (Fig. 12c and d). Besides, early pyrites, and in
500 particular framboids, preserved their trace elements signature, which is emphasized
501 by (Cu,As,Ni)-rich clusters in massive pyrites. Isotopic analyses on late metamorphic
502 pyrites yield $\delta^{34}S$ values between 9 and 15‰ (Fig. 13).

503

504 ***4.5.3. Uranium mineralogical expression and metamorphism***

505 Apatite-(CaF[OH]) nodules can also be found in metamorphic Alum Shale,
506 but they are more porous than in non metamorphic samples (Fig. 14e). Bell-shaped
507 REE spectra are flattened with a preferential enrichment in light and heavy REE (La,
508 Ce, Tm, Yb, Lu) compared to middle REE (Fig. 15b). Some of them display a negative
509 anomaly in Eu. Besides, whereas uranium concentration in non metamorphic shales
510 does not exceed a few hundreds ppm, it can reach several thousands ppm uranium
511 in metamorphic black schists (between 322 and 2655 ppm uranium).

512 As previously mentioned, no detectable uranium mineral was observed in
513 immature Alum Shale. On the contrary, in metamorphic Alum Shale, two types of
514 uranium bearing-minerals were detected: (a) uraninite and uranium titanate micro-
515 inclusions in synmetamorphic pyrites (Fig. 22a and b); (b) complex assemblages of U,
516 Ti, and Y phospho-silicates (Fig. 22c to f). In details, preserved uraninites and

517 uranium titanates are rare and can only be found in euhedral pyrites and
518 overgrowths associated with retrograde metamorphism. These pyrites are the latest
519 to crystallize around preexisting sulfides and pyrobitumens (Lecomte *et al.*, 2013). On
520 the contrary, uranium phospho-silicates are frequently found disseminated in the
521 organo-mineral matrix or in patches around pyrobitumen veins, pseudo-vitrinite
522 particles or pyrite. Uranium phospho-silicates seem to crystallize essentially at the
523 periphery of carbonaceous particles and on pyrite framboids. Rare occurences show
524 particular textures with uraninite or urano-titanates cores rimmed by U-Ti phospho-
525 silicates. Corrosion gulfs around these U-Ti oxides are also filled with U-Ti phospho-
526 silicates. Spherolites of uranium phospho-silicates were also found in apatite-
527 (CaF[OH]) nodules. In metamorphic Alum Shale, these porous phosphates nodules
528 are often surrounded by pyrobitumen. Uranium minerals have been analyzed with
529 electronic microprobe and standard-calibrated SEM (Table 8). All these
530 phosphosilicate clusters correspond to phosphocoffinites with variable Ti, Y, Zr
531 content.
532 Uranium phospho-silicates have variable analytical totals between 70 and 98.33 wt.%.
533 Low analytical totals in (phospho)-coffinite are probably related to micro-porosity or
534 hydratation (Deditius *et al.*, 2008). Atoms per formula units (APFU) of Si, P, Ca, Pb,
535 Ti, U, Y and Zr in uranium minerals were calculated on the basis of two oxygens and
536 one cation (Table 8). Three groups can be separated based on Y and Ti concentration:
537 (a) Y-poor/Ti-rich phospho-silicates ("Brannerite" group); (b) Y-poor/Ti-poor
538 phospho-silicates ("Uraninite" group); (c) Y-rich/Ti-poor phospho-silicates
539 ("Xenotime" group), including micro-spherolites apatite-(CaF[OH]) nodules. In

figure 23, Ti and U+Pb+Zr concentrations are plotted against Si and P content, respectively. Uraninite (UO_2), brannerite ($U_{0,33}Ti_{0,66}O_2$), coffinite ($U_{0,5}Si_{0,5}O_2$) and xenotime ($Y_{0,5}P_{0,5}O_2$) are also indicated. Pb and Zr content is low and these two elements are substituted for U in phospho-silicates. Pb and Zr will thus be considered with U concentration in successive graphs. Y-poor/Ti-rich phospho-silicates are aligned between "brannerite" and "coffinite" end-members, the former corresponding to well-preserved U-Ti oxides micro-inclusions in pyrite. Y-poor/Ti-poor phospho-silicates are aligned between "uraninite" and "coffinite" end-members, the former corresponding to well-preserved U oxides micro-inclusions in pyrite; the gap between analyses and theoretical evolution is caused by the presence of calcium in U phospho-silicates. Y-rich/Ti-poor phospho-silicates are aligned between "brannerite" and "coffinite" end-members, the former corresponding to rare YPO_4 crystals. Ca content is generally constant, whatever the concentration in Si, but increases along with P, only in the case of Y-poor/Ti-poor phospho-silicates ("uraninite").

5. Discussion

5.1. Sedimentation and uranium preconcentration

Sulfur, mainly present as sulfide, and organic carbon contents (Fig. 5a) provide different information on conditions of sedimentation for the Alum Shale of Sweden. In Carbon-Sulfur plots, marine sediments deposited in oxygenated waters display a positive correlation fitting the origin of the diagram. Indeed, pyrite precipitation occurs below the sediment-water interface and is limited by the

563 concentration of organic carbon (Berner and Raiswell, 1983). On the contrary,
564 sediments deposited in euxinic conditions would not display any correlation or
565 would have a positive intercept with the total sulfur axis (Raiswell and Berner, 1985).
566 This positive intercept represents the formation of pyrite in the water column and at
567 the sediment-water interface, regardless of the organic carbon content. The slightly
568 positive correlation line and the presence of data points in the "normal marine
569 sediments" field can be explained by euxinic conditions, but where pyrite
570 precipitation is limited by the concentration of available iron (Lyons and Berner,
571 1992; Leventhal, 1995). Besides, the evolution of the V/Cr ratio as a function of V/(V
572 +Ni) allows characterizing the level of oxygenation during sedimentation (Jones and
573 Manning, 1994; Hatch and Leventhal, 1992). For the Alum Shale Formation (Fig. 5b),
574 V/Cr and V/(V+Ni) ratios indicate sedimentation in suboxic to anoxic conditions.
575 During sedimentation, organic matter was accumulated as fluorescent liptinite
576 macerals and non-fluorescent pseudo-vitrinite macerals. However, vitrinite derived
577 from humification of vascular plants cannot exist in pre-silurian sediments. In fact,
578 pseudo-vitrinite is frequently observed in Cambrian Scandinavian shales (Kisch,
579 1980, Buchardt *et al.*, 1990) or in Tarim basin sediments (China) and may originate
580 from multicellular benthic algae (Wang, 2000). In the Alum Shale Formation, pseudo-
581 vitrinite and graptolites display identical reflectance, which suggests that vitrinite-
582 like particles may in fact be fragments of graptolites (Petersen *et al.*, 2013). Therefore,
583 petrographic observations are consistent with Rock-Eval analyses and support
584 organic matter accumulation in marine settings (Type II kerogens, Figures 8 and 9).
585 In the Alum Shale Formation, five successive pyrite generations (Py1 to Py5,

586 Fig. 13) precipitated during sedimentation and diagenesis. No particular trace-
587 element enrichment was measured in pyrites, which may indicate similar
588 geochemical conditions or low availability in interstitial fluids during sulfide
589 precipitation. High Cu and As content in framboids may be linked to specific affinity
590 of some trace elements (Mo, As, Cu), due to fast nucleation and high specific surface
591 of framboids.

592 The wide spread of $\delta^{34}S$ values in syn-sedimentary to syn-diagenetic pyrites
593 (-10 to +40‰; data from Dahl, 1990 and this study in Fig. 13) together with the
594 existence of negative values suggest the implication of bacterial processes resulting in
595 sulfate reduction and sulfide precipitation (Fig. 24).

596 When looked in details, disseminated framboids display negative $\delta^{34}S$ (-4‰
597 measured in this study). Negative values measured by Dahl (1990) on whole-rock
598 pyrites may thus be explained by the predominance of framboids over other pyrites
599 generations. Bacterial sulfate reduction (BSR) is known to produce ^{32}S-rich sulfides
600 compared to initial sulfate (Goldhaber *et al.,* 1978). Indeed, while inorganic sulfate
601 reduction yield a 22‰ sulfate-sulfide isotope fractionation (Harrison and Thode,
602 1958), bacterial pathway is responsible for higher fractionation, up to 46‰ on
603 bacterial cultures (Kaplan and Rittenberg, 1964) and 40‰ in sediments (Habicht and
604 Canfield, 2001 ; Canfield, 2001). Considering a $\delta^{34}S$ value of about 30‰ for initial
605 sulfate [$\delta^{34}S$ of SO_4^{2-} in marine Cambrian waters (Claypool *et al.,* 1980; Strauss, 1997),
606 the most likely sulfate source for early pyrites], such fractionation brings in $\delta^{34}S$
607 down to -15‰. Unlike disseminated framboids, cogenetic euhedral pyrites and
608 cemented framboids clusters form beds parallel to shale stratification and show

609 highly positive $\delta^{34}S$, above $\delta^{34}S$ of sulfate in marine Cambrian waters. Theoretically,
610 sulfate supply and availability are the main processes affecting isotope variability in
611 sedimentary sulfides. Indeed, considering an open system in which sulfate reservoir
612 is permanently replenished, isotope fractionation remains constant and yield to
613 negative $\delta^{34}S$ in the case of predominant bacterial sulfate reduction. On the contrary,
614 in a closed system, reduction of sulfate pool to sulfides preferentially removes ^{32}S
615 and thus enriches residual sulfate in ^{34}S. Sulfides show higher and higher $\delta^{34}S$ which
616 tend towards value of starting sulfate. However, even in an ideally closed system,
617 sulfide $\delta^{34}S$ cannot exceed $\delta^{34}S$ of initial sulfate, due to mass conservation between
618 ^{32}S and ^{34}S once sulfate is depleted. Jørgensen (2004) even considers that such a
619 distinction between open and closed systems cannot be applied to marine sediments
620 because: (a) it passes over vertical diffusion processes of SO_4^{2-} and H_2S in the
621 sediment, and particularly the fact that isotope ratios of these fluxes differ from those
622 of SO_4^{2-} and H_2S reservoirs at different depths; (b) most present-day sediments used
623 as analogues, including in anoxic closed basins such as Black Sea, cannot be
624 considered as truly closed systems because they are never completely isolated from
625 seawater sulfate reservoir. Moreover, in the case of the Alum Shale Formation,
626 precipitation of disseminated framboids or micro-pyrites, beds of euhedral pyrites
627 and framboids clusters is probably very early, in the water column, at water-
628 sediment interface or within first centimeters of the sediment. Therefore, isotope
629 composition of sulfides precipitated in sediment and in particular progressive $\delta^{34}S$
630 enrichment do not seem to be related to the development of a closed system, but
631 rather to fractionation and vertical diffusion of SO_4^{2-} and H_2S with a $\delta^{34}S$ enrichment

of interstitial water sulfates. This model is based on isotopic measurement of sulfides from the Black Sea, in which pyrites that precipitated in the water column have positive $\delta^{34}S$, sometimes close to $\delta^{34}S$ of initial sulfate pool (Lyons and Berner, 1992; Wilkin and Arthur, 2001). Jørgensen (2004) thus demonstrated important $\delta^{34}S$ enrichment of SO_4^{2-} and H_2S toward sediment depth. This is not related to the development of a closed system s.s. but to a steeper gradient for ^{32}S than for ^{34}S, which yields larger ^{32}S depletion and thus ^{34}S-rich remaining sulfate at depth. Such a process may generate sulfates with extreme $\delta^{34}S$, up to +135‰ 40 meters below sediment-water interface (Rudnicki *et al.*, 2001). Moreover, elevated gradients can yield $\delta^{34}S$ increase of 40‰ within 2-3 meters and 70‰ within 15-20 meters in the sediment. On the contrary, H_2S gradient is steeper for ^{34}S than for ^{32}S. These gradients have important consequences for sulfate and sulfide diffusion in the sediment (Jørgensen, 1979; Goldhaber and Kaplan, 1980; Chanton *et al.*, 1987). Indeed, compared with interstitial waters at the same depth, downward SO_4^{2-} flux is enriched in ^{32}S and upward H_2S flux is enriched in ^{34}S. This differential diffusion, although limited in comparison with sulfate and sulfide concentrations in modern sediments (Jørgensen, 2004) implies: (1) ^{32}S transfer toward depth and therefore limitation of $\delta^{34}S$ increase in deep sulfates; (2) light sulfide conservation at depth and heavy H_2S flux toward surface. The behavior and evolution of isotopic ratios sulfates and sulfides in sediments is a complex system that cannot be reduced to the differentiation between an open system and closed system.

In the Alum Shale Formation, with an increase in the first meters of the sediment as previously described, $\delta^{34}S$ values of interstitial water sulfates may reach

655 70 to 80‰, and lead to high $\delta^{34}S$ in sedimentary pyrites through bacterial sulfate
656 reduction (30-40‰ in pyrite clusters and beds of first generation). In that case,
657 framboids with negative $\delta^{34}S$ should be considered as the earliest pyrites precipitated
658 through BSR in the water column or at the sediment-water interface, from a primary
659 sulfate pool (seawater sulfate). Second and third pyrite generations have close $\delta^{34}S$
660 values between 18 and 26‰, lower than early pyrites. Petrographically, some of
661 these pyrites correspond to recrystallization of cemented early pyrites, and their
662 signature may therefore be a mixing between negative $\delta^{34}S$ of framboids and high
663 $\delta^{34}S$ of euhedral pyrites. The large pyrite crystals, which remain disseminated in the
664 shale or grow perpendicular to some pyrite band and form centimeter-scale beds and
665 nodules, have very similar $\delta^{34}S$ around 24-25 ‰. Besides, no differences in isotope
666 ratio were measured between the base (or core) and the top (or edge) of the crystals,
667 which would indicate a homogeneous growth phase. However, a massive pyrite
668 with an early pyrite inclusion display a $\delta^{34}S$ increase from core to rim (16 to 23‰).
669 Therefore, after crystallization of high-$\delta^{34}S$ primary pyrites ($\delta^{34}S$ = 30-40‰), a phase
670 of cementation and crystal growth occurred, with $\delta^{34}S$ around 15-16‰. This phase is
671 followed by progressive ^{34}S enrichment of residual sulfate, either locally through
672 closed system Rayleigh fractionation or with sulfate $\delta^{34}S$ increase with depth. The
673 fourth pyrite generation, which correspond to massive pyrite cementation, may be
674 the end of ^{34}S enrichment process with $\delta^{34}S$ around 30-31‰, close to that of sulfates
675 in Cambrian marine waters.

676 Although $\delta^{34}S$ evolution of pyrite generation can be explained by progressive
677 enrichment of sulfates in ^{34}S, the 15-25‰ drop of $\delta^{34}S$ between early pyrites

678 precipitated in the sediment and the second generation of pyrite, which cements
679 detrital grains and early pyrites, remains unclear. Considering similar isotope
680 fractionation for the first four generations precipitated in non-indurated sediment,
681 the best explanation implies supply of light sulfate from overlying seawater during
682 reworking of superficial sediment, which would have brought a 20‰ decrease of the
683 δ34S of interstitial water sulfate. In the same way, the fifth generation of pyrite is
684 characterized by a 10‰ drop of the $\delta^{34}S$, although being the latest generation in a
685 general trend of increasing $\delta^{34}S$. These pyrites, which correspond to fracture fillings
686 in the shale and overgrowths in fractures within massive pyrites, precipitated during
687 late diagenesis at temperatures between 50 and 100-120°C (maximum temperature
688 indicated by fluorescence colors of macerals). One possible explanation involves light
689 H_2S generated by kerogen thermal maturation in the most mature Alum Shale
690 (Amrani *et al.,* 2005). Besides, bacterial activity and bacterial sulfate reduction is
691 generally possible at temperatures below 80°C (Machel, 2001), and rarely up to 110°C
692 (Jørgensen, 1992). Considering, maximum temperatures suggested by kerogens, it is
693 thus necessary to take into account potential influence of thermochemical sulfate
694 reduction (TSR) occurring at temperatures above 100°C (Machel, 2001; Basuki *et al.,*
695 2008). TSR can theoretically yield isotope fractionation between 0 and -20‰ (Machel,
696 1995). Indeed, whereas TSR experimental reproduction brings fractionation between
697 10 and 20‰ (Harrison and Thode, 1957; Kiyosu and Krouse, 1990), in most
698 sedimentary deposits no fractionation is measured (Krouse, 1977; Orr, 1977; Worden
699 and Smalley, 1996; Cai *et al.,* 2001). Therefore, the last generation of pyrite may also
700 precipitate through TSR of sulfates showing a $\delta^{34}S$ around 20-30‰.

In immature Alum Shale, uranium mineralization has no expression as even discrete mineral phases. However, uranium concentration is positively correlated with organic carbon content (Fig. 6a) and phosphorus concentration (Fig. 6b), indicating a specific association where uranium shows a dissemination and/or a complexation with organic matter or phosphates. Such a close relationship was previously suggested by several studies on *kolm*, organic matter lenses containing up to several thousands ppm uranium, in particular in cerium-bearing minerals (Cobb and Kulp, 1961; Armands, 1972; Parnell, 1984).

The correlation between phosphorus and uranium contents in Alum Shale is linked to the existence of a major uranium-bearing phase as calcium phosphate nodules. These apatite-(CaF[OH]) nodules are disseminated in the black shale and show typical bell-shaped REE patterns, with a strong enrichment in middle REE. This type of pattern is common in marine sediments, particularly in pre-Jurassic biogenic phosphates, and can be explained by two successive processes: an adsorption mechanism during early diagenesis and a substitution mechanism associated with recrystallization during late diagenesis (Reynard *et al.*, 1999). These apatite-(CaF[OH]) nodules contain 100 to 3000 ppm uranium and therefore constitute an important part of uranium mineralization (Fig. 25). However, the projection of whole-rock U concentration to the 18% phosphorus content typical of apatite, indicates that apatite in the Alum Shale could contain up to 1500 $\mu g.cm^{-3}$ uranium (i.e. around 600 ppm U). This result suggests that only uranium content below 600 ppm in phosphate nodules corresponds to the primary homogeneous preconcentration associated with sedimentation and diagenesis, whereas higher

724 values may indicate local reconcentration as phosphosilicate spherolites (Fig. 25).

725

726 **5.2. Burial and thermal maturation**

727 During burial and thermal maturation, Alum Shale generated hydrocarbons
728 that were trapped as fluid inclusions in carbonate levels within the black shale and in
729 fractured Ordovician limestones. Petroleum and aqueous isochores indicate high
730 trapping temperature (>150°C) and extremely variable trapping pressure, from
731 700 bars for low-T_h inclusions to 200 bars for high-T_h inclusion (Fig. 26). Besides, P-T
732 domains seem to be aligned in a rather similar temperature range, which may
733 suggest isothermal decompression during calcite crystallization. Several theoretical
734 pathways are indicated on figure 26. First hypothesis considers an underestimated
735 burial with low geothermal gradient (<20°C/km), consistent with present-day
736 foreland basin gradients and suggested by Huigen and Andriessen (2004) for the
737 Caledonian foreland basin. In that case, high pressures could be reached but at
738 temperatures below 100°C. Second hypothesis uses a normal geothermal gradient to
739 obtain high pressure/high temperature conditions. Finally, a third hypothesis
740 considers a low burial to explain low trapping pressure of most inclusions in
741 concretions, but precludes high pressure conditions.

742 Alum Shale in central Sweden (Västergötland, Östergötland, Närke) is
743 immature and did not encountered temperatures above 90-100°C. Besides, Alum
744 Shale burial is mainly related to the development of a Silurian-Devonian foreland
745 basin during Caledonian orogeny (Ziegler, 1988; Middleton *et al.*, 1996). Basin
746 modeling (Samuelson and Middleton, 1998, 1999) indicates a 2 kilometers deep
747 maximum burial in central Sweden (Västergötland, Närke). Since the Caledonian

748 foreland basin gets thinner eastward, maximum burial during the Devonian ranges
749 between 1 and 2 kilometers at Åland (Cederbom, 1997 and Larson *et al.*, 1998, cited in
750 Larson *et al.*, 1999). The initial uplift, probably starting in the Devonian, is faster in
751 the western part of the basin. This implies lateral redistribution of the sediments
752 which leads to a rather uniform 2 kilometers deep basin infill around 250 Ma (Larson
753 *et al.*, 1999). Therefore, Alum Shale burial in central Sweden never exceeded 2
754 kilometers in the Devonian, and probably less in the Ordovician, because most post-
755 Cambrian accumulated sediments correspond to foreland basin filling during the
756 Silurian-Devonian period. U-Pb dating of cone-in-cone calcite indicates that
757 formation of late concretions in the Upper Cambrian Alum Shale took place during
758 Early Ordovician (Israelson *et al.*, 1996) at relatively limited depth. By analogy with
759 present-day geothermal gradients in hypothermal foreland basins and considering
760 the thermal age of basement rocks (Huigen and Andriessen, 2004), a low paleo-
761 geothermal gradient of 20°C/km seems to be realistic and implies that temperature
762 reached by most immature Alum Shale may not have exceeded a few tens of degrees.
763 Since concretions and fractures are pre-Permian, local thermal maturation related to
764 Permian dolerite intrusions cannot be considered as a major process of hydrocarbon
765 generation. Moreover, thermal influence of intrusions on Alum Shale is limited to a
766 few tens of meters (30 meters at Kinnekulle according to Samuelsson and Middleton,
767 1999), which excludes any significant influence of Permian intrusions on regional
768 heating at the end of the Palaeozoic (Tullborg *et al.*, 1996; Larson *et al.*, 1998).

769 Although it is not possible to completely rule out either overestimation of P-T
770 trapping conditions because of inclusion volume modification or underestimation of

771 maximum burial in particular considering extremely low thermal gradient, it seems
772 to be clear that theoretical pathways are unachievable with foreland basin evolution
773 and that formation of calcite concretions and fractures is related to the circulation of
774 overpressured and overheated fluids. Such concretions, described as bedding-
775 parallel veins or beefs, are indeed widespread in low-permeability strata in
776 sedimentary basins and generally contain solid or liquid hydrocarbons. Beefs may be
777 the result of fluid overpressure linked to petroleum generation (Cobbold *et al.*, 2013;
778 Rodrigues *et al.*, 2009). To explain the existence of beefs, concretions, breccias and
779 fractures containing hydrocarbons in immature areas, it is necessary to consider
780 contemporaneous migration of hydrocarbons and brines from mature and
781 overmature Alum Shale to immature Alum Shale. In that model, overpressure allows
782 fracture opening and calcite precipitation, which in turn induce fluid pressure drop.
783 These regional migrations are already active in the Ordovician and lead to primary
784 beef formation. First inclusions contain black oils with orange-brown fluorescence
785 and formed at high pressure (>500 bars) and high temperature (>150°C). Second
786 assemblage is characterized by a higher proportion of mature oils with white-blue
787 fluorescence. These inclusions are associated with numerous brine inclusions and
788 have been trapped around 150-170°C and 200 bars. This pressure drop is interpreted
789 as a decompression after fracture opening. Beefs have been locally dislocated and
790 reworked as breccias. Angular calcite particles preclude long-distance transport and
791 may suggest insitu reworking. Such breccias have only been observed at Öland, in a
792 more proximal environment than Västergötland or Närke. Fracture fillings in
793 Ordovician limestones are later. The presence of monophasic oil inclusions at room

794 temperature indicates high pressure trapping. Low-T_h inclusions have been trapped
795 at high pressure between 600 and 700 bars and temperatures around 200°C, whereas
796 high-T_h inclusions have been trapped around 400 bars and 170-180°C. Therefore,
797 fluid inclusions have recorded a major pressure drop of several hundreds of bars
798 between first opening of fractures by overpressured hydrocarbons and brines and
799 the final sealing. Temperature decrease is probably related to fluid cooling during
800 calcite precipitation within a rather cold host rock.

801 However, these fluids do not contain significant uranium concentration (see
802 section 4.4.1). Thermal maturation simulation (Dahl, 1990; this study) shows that
803 uranium remains immobile during maturation. In the meantime, carbon loss reaches
804 up to 10% or more (22% in this study) with the formation of 10% residual carbon
805 (Horsfield *et al.*, 1992). Thus, carbon loss during thermal maturation of Alum Shale
806 leads to a relative enrichment in uranium due to rock density changes in response to
807 the carbon loss, which may partly explain the steeper slope of the correlation line in
808 metamorphic samples compared to immature samples.

809

810 **5.3. Uranium remobilization during metamorphism**

811 During Caledonian orogeny, Alum Shale has been heated up to 305±11°C, as
812 recorded by organic material. This temperature corresponds to sub-greenshist
813 metamorphic facies, as previously suggested by Kisch (1980).

814 During metamorphism, uranium preconcentration is remobilized and
815 cristallized as uraninite or uranotitanate. Some micro-crystals remain preserved from
816 alteration as inclusions in metamorphic pyrites. Outside pyrites, uraninites and
817 urano-titanates are now replaced by U-Ti phospho-silicates clusters or rims around

818 U-Ti oxides primary cores. These phospho-silicates contain U, Ti, Y, Zr, Pb with
819 highly variable concentrations and can be gathered in three chemical groups: a) Y-
820 poor/Ti-rich phospho-silicates (“Brannerite” group); (b) Y-poor/Ti-poor phospho-
821 silicates (“Uraninite” group); (c) Y-rich/Ti-poor phospho-silicates (“Xenotime”
822 group). These distinct U-Ti phospho-silicate series result from silicification and/or
823 phosphorization of different mineral precursors, which can rarely be found
824 preserved throughout the Alum Shale. Y-poor/Ti-rich phospho-silicates result from
825 the silicification of brannerite. Silicification comes along a drop in Ti content,
826 associated with TiO_2 crystallization, whereas U concentration remains constant. Y-
827 poor/Ti-poor phospho-silicates result from the silicification of uraninite, with
828 U ↔ Ca and Si ↔ P substitutions. In this series, Y concentration remains low. Finally,
829 Y-rich/Ti-poor phospho-silicates result from the silicification of Y-phosphate, with
830 Y ↔ U and P ↔ Si substitutions. During Greenschist facies metamorphism, uranium
831 can also be redistributed in sedimentary apatite-(CaF[OH]) nodules. U
832 concentrations above 600 ppm thus correspond to reconcentration areas with local
833 crystallization of phosphosilicate micro-spherulites.
834

835 ## 6. Conclusions

836 Scandinavian Alum Shale is among the most uraniferous black shale units
837 throughout Earth history and extends over most of northern Europe. As in many
838 other black shales, uranium was preconcentrated during sedimentation. In the Alum
839 Shale Formation, uranium primary accumulation occurred in organic matter and
840 biogenic marine phosphate nodules. Besides, it is clear that primary concentration

841 has not been affected by early burial, thermal maturation of organic matter and
842 petroleum generation. Migrating fluids in the Alum Shale Formation did not carry
843 any particular uranium content. However, uranium was remobilized during
844 Greenschist facies metamorphism of Caledonian orogeny and crystallized as
845 uraninite and brannerite minerals. Rare remnants of this crystallization stage are
846 found as micro-inclusions in syn-metamorphic pyrites. Most of mineralization
847 actually evolved to complex U-Ti phospho-silicates, as clusters associated with
848 carbonaceous matter or spherulites inside biogenic phosphate nodules.

849 This work shows that, despite its relatively high synsedimentary
850 preconcentration, uranium remains immobile through the stages of diagenesis, burial
851 and thermal maturation. However, pressure-temperature conditions reached during
852 Caledonian orogeny are high enough to favor new uranium speciation as U-Ti oxides
853 and phospho-silicates. The knowledge of uranium mineralogy and its particular
854 association with phosphates is crucial to assess potential extraction feasibility and
855 adjust recovery processes. This result is also of great interest for the oil and gas
856 companies prospecting hydrocarbons in southern Sweden Alum Shale. Thus,
857 uranium could be considered to have a potential penalizing effect on the quality of
858 released waters during the gas recovery by hydrofracturing. But, as it occurs up to
859 the oil window as poorly soluble phosphates, the risks of potential water
860 contamination by radionuclides are probably minimized.

861

862 ## Acknowledgments

863 The authors would like to thank M. Hudson (Mawson Resources) and C.

Caillat (AREVA) for helping us during this study and for their assistance during the field trip in Sweden. We are grateful to the Geological Survey of Sweden (SGU), especially L. Hildebrand and L. Wickström, for welcoming us in Malå and Uppsala and for their technical assistance in the sampling process. We acknowledge Niels H. Schovsbo for his useful comments and suggestions.

This work was supported by Institut Carnot Énergie et Environnement en Lorraine (ICEEL), Labex Ressources 21 (supported by the French National Research Agency through the national program "Investissements d'avenir", reference ANR-10-LABX-21–LABEX RESSOURCES 21) and AREVA.

875 ## References

876 Amrani, A., Lewan, M.D., Aizenshtat, Z., 2005. Stable sulfur isotope partitioning
877 during simulated petroleum formation as determined by hydrous pyrolysis
878 of Ghareb Limestone, Israel. Geochimica et Cosmochimica Acta 69, 5317–
879 5331.

880 Andersson, A., Dahlman, B., Gee, D.G., Snäll, S., 1985. The Scandinavian Alum
881 Shales. Sveriges Geologiska Undersökning, Uppsala.

882 Armands, G., 1972. Geochemical studies of uranium, molybdenum and vanadium in
883 a Swedish alum shale. Stockholm University.

884 Berner, R.A., Raiswell, R., 1983. Burial of organic carbon and pyrite sulphur in
885 sediments over Phanerozoic time: a new theory. Geochimica et
886 Cosmochimica Acta 47, 855– 862.

887 Beyssac, O., Brunet, F., Petitet, J.-P., Goffé, B., Rouzaud, J.-N., 2003a. Experimental
888 study of the microtextural and structural transformations of carbonaceous
889 materials under pressure and temperature. European Journal of Mineralogy
890 15, 937–951.

891 Beyssac, O., Goffé, B., Chopin, C., Rouzaud, J.N., 2002. Raman spectra of
892 carbonaceous material in metasediments: a new geothermometer. Journal of
893 Metamorphic Geology 20, 859–871.

894 Beyssac, O., Goffé, B., Petitet, J.-P., Froigneux, E., Moreau, M., Rouzaud, J.-N., 2003b.
895 On the characterization of disordered and heterogeneous carbonaceous
896 materials by Raman spectroscopy. Spectrochimica Acta Part A: Molecular
897 and Biomolecular Spectroscopy 59, 2267–2276.

898 Beyssac, O., Lazzeri, M., 2012. Application of Raman spectroscopy to the study of
899 graphitic carbons in the Earth Sciences, in: Dubessy, J., Caumon, M.-C.,
900 Rull, F. (Eds.), Applications of Raman Spectroscopy to Earth Sciences and
901 Cultural Heritage, EMU Notes in Mineralogy. European Mineralogical
902 Union and the Mineralogical Society of Great Britain & Ireland, pp. 415–454.
903 Buchardt, B., Schovsbo, N.H., Nielsen, A.T., 1997. Alun skiferen i Skandinavien.
904 Geologisk Tidsskrift 3, 1–30.
905 Canfield, D.E., 2001. Isotope fractionation by natural populations of sulfate-reducing
906 bacteria. Geochimica et Cosmochimica Acta 65, 1117–1124.
907 Cederbom, C., 1997. Fission track thermochronology applied to Phanerozoic
908 thermotectonic events in central and southern Sweden. PhD Thesis, Earth
909 Sciences Centre, Göteborg University, Earth Sciences Centre.
910 Chanton, J.P., Martens, C.S., Goldhaber, M.B., 1987. Biogeochemical cycling in an
911 organic-rich coastal marine basin. 8. A sulfur isotopic budget balanced by
912 differential diffusion across the sediment-water interface. Geochimica et
913 Cosmochimica Acta 51, 1201–1208.
914 Claypool, G.E., Holser, W.T., Kaplan, I.R., Sakai, H., Zak, I., 1980. The age curves of
915 sulfur and oxygen isotopes in marine sulfate and their mutual
916 interpretation. Chemical Geology 28, 199–260.
917 Cobb, J.C., Kulp, J.L., 1961. Isotopic geochemistry of uranium and lead in the
918 Swedish kolm and its associated shale. Geochimica et Cosmochimica Acta
919 24, 226–249.
920 Cobbold, P.R., Zanella, A., Rodrigues, N., Løseth, H., 2013. Bedding-parallel fibrous

921 veins (beef and cone-in-cone): Worldwide occurrence and possible
922 significance in terms of fluid overpressure, hydrocarbon generation and
923 mineralization. Marine and Petroleum Geology 43, 1–20.
924 Dahl, J., 1990. The organic geochemistry of the Alum Shale, Sweden. University of
925 California, Los Angeles.
926 Deditius, A.P., Utsunomiya, S., Ewing, R.C., 2008. The chemical stability of coffinite,
927 $USiO_4 \cdot nH_2O$; $0<n<2$. Chemical Geology 251, 33–49.
928 Dubessy, J., Lhomme, T., Boiron, M.-C., Rull, F., 2002. Determination of Chlorinity in
929 Aqueous Fluids Using Raman Spectroscopy of the Stretching Band of Water
930 at Room Temperature: Application to Fluid Inclusions. Applied
931 Spectroscopy 56, 99–106.
932 Goldhaber, M.B., Kaplan, I.R., 1980. Mechanisms of sulfur incorporation and isotope
933 fractionation during early diagenesis in sediments of the gulf of California.
934 Marine Chemistry 9, 95–143.
935 Goldhaber, M.B., Reynolds, R.L., Rye, R.O., 1978. Origin of a South Texas roll-type
936 uranium deposit; II, Sulfide petrology and sulfur isotope studies. Economic
937 Geology 73, 1690–1705.
938 Gromet, L.P., Haskin, L.A., Korotev, R.L., Dymek, R.F., 1984. The "North American
939 shale composite": Its compilation, major and trace element characteristics.
940 Geochimica et Cosmochimica Acta 48, 2469–2482.
941 Habicht, K.S., Canfield, D.E., 2001. Isotope fractionation by sulfate-reducing natural
942 populations and the isotopic composition of sulfide in marine sediments.
943 Geology 29, 555–558.

944 Harrison, A.G., Thode, H.G., 1958. Mechanism of the bacterial reduction of sulfate
945 from isotopic fractionation studies. Trans. Faraday Soc. 54, 84–92.
946 Hatch, J.R., Leventhal, J.S., 1992. Relationship between inferred redox potential of the
947 depositional environment and geochemistry of the Upper Pennsylvanian
948 (Missourian) stark shale member of the Dennis Limestone, Wabaunsee
949 County, Kansas, USA. Chemical Geology 99, 65–82.
950 Holland, H.D., 1979. Metals in black shales; a reassessment. Economic Geology 74,
951 1676–1680.
952 Horsfield, B., Bharati, S., Larter, S.R., Leistner, F., Littke, R., Schenk, H.J., Dypvik, H.,
953 1992. On the Atypical Petroleum-Generating Characteristics of Alginite in
954 the Cambrian Alum Shale, in: Schidlowski, M., Golubic, S., Kimberley, M.,
955 McKirdy, D., Sr., Trudinger, P.A. (Eds.), Early Organic Evolution. Springer
956 Berlin Heidelberg, pp. 257–266.
957 Huigen, Y., Andriessen, P., 2004. Thermal effects of Caledonian foreland basin
958 formation, based on fission track analyses applied on basement rocks in
959 central Sweden. Physics and Chemistry of the Earth 29, 683-694.
960 Israelson, C., Halliday, A.N., Buchardt, B., 1996. U-Pb dating of calcite concretions
961 from Cambrian black shales and the Phanerozoic time scale. Earth and
962 Planetary Science Letters 141, 153–159.
963 Jones, B., Manning, D.A.C., 1994. Comparison of geochemical indices used for the
964 interpretation of palaeoredox conditions in ancient mudstones. Chemical
965 Geology 111, 111–129.
966 Jørgensen, B.B., 1979. A theoretical model of the stable sulfur isotope distribution in

967 marine sediments. Geochimica et Cosmochimica Acta 43, 363–374.
968 Jørgensen, B.B., Böttcher, M.E., Lüschen, H., Neretin, L.N., Volkov, I.I., 2004.
969 Anaerobic methane oxidation and a deep H2S sink generate isotopically
970 heavy sulfides in Black Sea sediments. Geochimica et Cosmochimica Acta
971 68, 2095–2118.
972 Jørgensen, B.B., Isaksen, M.F., Jannasch, H.W., 1992. Bacterial sulfate reduction above
973 100°C in deep-sea hydrothermal vent sediments. Science 258, 1756–1757.
974 Kaplan, I.R., Rittenberg, S.C., 1964. Microbiological Fractionation of Sulphur
975 Isotopes. J Gen Microbiol 34, 195–212.
976 Kisch, H.J., 1980. Incipient metamorphism of Cambro-Silurian clastic rocks from the
977 Jämtland Supergroup, Central Scandinavian Caledonides, Western Sweden:
978 Illite crystallinity and "vitrinite" reflectance. Journal of the Geological
979 Society 137, 271–288.
980 Lahfid, A., Beyssac, O., Deville, E., Negro, F., Chopin, C., Goffé, B., 2010. Evolution of
981 the Raman spectrum of carbonaceous material in low-grade metasediments
982 of the Glarus Alps (Switzerland). Terra Nova 22, 354–360.
983 Langford, F.F., Blanc-Valleron, M.M., 1990. Interpreting Rock-Eval pyrolysis data
984 using graphs of pyrolyzable hydrocarbons vs. total organic carbon. AAPG
985 Bulletin 74, 799–804.
986 Larson, S.A., Tullborg, E.L., Cederbom, C., Stiberg, J.P., Björklund, P.P., Björklund, L.,
987 1999. The Caledonian foreland basin in Scandinavia: Constrained by the
988 thermal maturation of the alum shale. A discussion. GFF 121, 155–156.
989 Larson, S.A., Tullborg, E.L., Stiberg, J.P., Cederbom, C., 1998. Phanerozoic

990 sedimentation and erosion in Sweden and Finland - New results from
991 fission track analyses, in: 23 Nordiske Geologiske Vintermøde.
992 Lecomte, A., Cathelineau, M., Deloule, E., Brouand, M., Peiffert, C., Loukola-
993 Ruskeeniemi, K., Pohjolainen, E., Lahtinen, H., 2014. Uraniferous bitumen
994 nodules in the Talvivaara Ni-Zn-Cu-Co deposit (Finland): influence of
995 metamorphism on uranium mineralization in black shales. Mineralium
996 Deposita 49, 513–533.
997 Lecomte, A., Cathelineau, M., Michels, R., Brouand, M., 2013. Uranium
998 mineralization in the Alum Shale Formation (Sweden), in: Jonsson, E. (Ed.),
999 12th Biennial SGA Meeting - Mineral Deposit Research for a High-Tech
1000 World. pp. 1654–1656.
1001 Leisen, M., 2011. Analyse chimique des inclusions fluides par ablation-laser couplée à
1002 l'ICP-MS et applications géochimiques. Nancy-Université,.
1003 Leventhal, J.S., 1995. Carbon-sulfur plots to show diagenetic and epigenetic
1004 sulfidation in sediments. Geochimica et Cosmochimica Acta 59, 1207–1211.
1005 Lewis, S., Henderson, R., Dickens, G., Shields, G., Coxhell, S., 2010. The geochemistry
1006 of primary and weathered oil shale and coquina across the Julia Creek
1007 vanadium deposit (Queensland, Australia). Mineralium Deposita 45, 599–
1008 620.
1009 Lippmaa, E., Maremäe, E., Pihlak, A.T., 2011. Resources, production and processing
1010 of baltoscandian multimetal black shales. Oil Shale 28, 68–77.
1011 Lyons, T.W., Berner, R.A., 1992. Carbon– sulfur– iron systematics of the uppermost
1012 deep-water sediments of the Black Sea. Chemical Geology 99, 1–27.

1013 Machel, H.G., 2001. Bacterial and thermochemical sulfate reduction in diagenetic
1014 settings -- old and new insights. Sedimentary Geology 140, 143–175.
1015 Middleton, M.F., Tullborg, E.L., Larson, S.A., Björklund, L., 1996. Modelling of a
1016 Caledonian foreland basin in Sweden: Petrophysical constraints. Marine
1017 and Petroleum Geology 13, 407–413.
1018 Montel, F., 1993. Phase equilibria needs for petroleum exploration and production
1019 industry. Fluid Phase Equilibria 84, 343–367.
1020 Nemanich, R.J., Solin, S.A., 1979. First- and second-order Raman scattering from
1021 finite-size crystals of graphite. Physical Review B 20, 392–401.
1022 Nielsen, A.T., Schovsbo, N.H., 2006. Cambrian to basal Ordovician lithostratigraphy
1023 in southern Scandinavia. Bulletin of the Geological Society of Denmark 53,
1024 47-92.
1025 Nielsen, A.T., Schovsbo, N.H., 2011. The Lower Cambrian of Scandinavia:
1026 Depositional environment, sequence stratigraphy and palaeogeography.
1027 Earth-Science Reviews 107, 207–310.
1028 Nielsen, A.T., Schovsbo, N.H., 2015. The regressive Early-Mid Cambrian "Hawke
1029 Bay Event" in Baltoscandia: Epeirogenic uplift in concert with eustasy.
1030 Earth-Science Reviews 151, 288–350.
1031 Parnell, J., 1984. The distribution of uranium in kolm: Evidence from backscattered
1032 electron imagery. Geologiska Föreningen i Stockholm Förhandlingar 106,
1033 231–234.
1034 Pearce, N.J.G., Perkins, W.T., Westgate, J.A., Gorton, M.P., Jackson, S.E., Neal, C.R.,
1035 Chenery, S.P., 1997. A compilation of new and published major and trace

element data for NIST SRM 610 and NIST SRM 612 glass reference materials. Geostandards Newsletter-the Journal of Geostandards and Geoanalysis 21, 115–144.

Petersen, H.I., Schovsbo, N.H., Nielsen, A.T., 2013. Reflectance measurements of zooclasts and solid bitumen in Lower Paleozoic shales, southern Scandinavia: Correlation to vitrinite reflectance. International Journal of Coal Geology 114, 1–18.

Pironon, J., Canals, M., Dubessy, J., Walgenwitz, F., Laplace-Builhe, C., 1998. Volumetric reconstruction of individual oil inclusions by confocal scanning laser microscopy. European Journal of Mineralogy 10, 1143–1150.

Pironon, J., Thiery, R., Ayt Ougougdal, M., Teinturier, S., Beaudoin, G., Walgenwitz, F., 2001. FT-IR measurements of petroleum fluid inclusions: methane, n-alkanes and carbon dioxide quantitative analysis. Geofluids 1, 2–10.

Raiswell, R., Berner, R.A., 1985. Pyrite formation in euxinic and semi-euxinic sediments. American Journal of Science 285, 710–724.

Reynard, B., Lécuyer, C., Grandjean, P., 1999. Crystal-chemical controls on rare-earth element concentrations in fossil biogenic apatites and implications for paleoenvironmental reconstructions. Chemical Geology 155, 233–241.

Rodrigues, N., Cobbold, P.R., Loseth, H., Ruffet, G., 2009. Widespread bedding-parallel veins of fibrous calcite ('beef') in a mature source rock (Vaca Muerta Fm, Neuquén Basin, Argentina): evidence for overpressure and horizontal compression. Journal of the Geological Society 166, 695–709.

Rudnicki, M.D., Elderfield, H., Spiro, B., 2001. Fractionation of sulfur isotopes during

1059 bacterial sulfate reduction in deep ocean sidements at elevated
1060 temperatures. Geochimica et Cosmochimica Acta 65, 777–789.
1061 Samuelsson, J., Middleton, M.F., 1999. The Caledonian foreland basin in Scandinavia:
1062 Constrained by the thermal maturation of the Alum Shale. A reply. GFF
1063 121, 157–159.
1064 Samuelsson, J., Middleton, M.F., 1998. The Caledonian foreland basin in Scandinavia:
1065 Constrained by the thermal maturation of the Alum Shale. GFF 120, 307–
1066 314.
1067 Schovsbo, N.H., 2002. Uranium enrichment shorewards in black shales: A case study
1068 from the Scandinavian Alum Shale. GFF 124, 107–115.
1069 Schovsbo, N.H., Nielsen, A.T., Klitten, K., Mathiesen, A., Rasmussen, P., 2011. Shale
1070 gas investigations in Denmark: Lower Palaeozoic shales on Bornholm.
1071 Geological Survey of Denmark & Greenland Bulletin 23, 09-12.
1072 Scotese, C.R., McKerrow, W.S., 1990. Revised World maps and introduction.
1073 Geological Society, London, Memoirs 12, 1–21.
1074 Strauss, H., 1997. The isotopic composition of sedimentary sulfur through time.
1075 Palaeogeography, Palaeoclimatology, Palaeoecology 132, 97–118.
1076 Sundblad, K., Gee, D.G., 1984. Occurrence of a uraniferous-vanadiniferous graphitic
1077 phyllite in the Köli Nappes of the Stekenjokk area, central Swedish
1078 Caledonides. Geologiska Föreningen i Stockholm Förhandlingar 106, 269–
1079 274.
1080 Thickpenny, A., 1984. The sedimentology of the Swedish Alum Shales. Geological
1081 Society, London, Special Publications 15, 511–525.

1082 Thiéry, R., Pironon, J., Walgenwitz, F., Montel, F., 2000. PIT (Petroleum Inclusion
1083 Thermodynamic): a new modeling tool for the characterization of
1084 hydrocarbon fluid inclusions from volumetric and microthermometric
1085 measurements. Journal of Geochemical Exploration 69–70, 701–704.
1086 Tissot, B.P., Welte, D.H., 1984. Petroleum Formation and Occurence. Springer Verlag.
1087 Tuinstra, F., Koenig, J.L., 1970. Raman Spectrum of Graphite. The Journal of
1088 Chemical Physics 53, 1126–1130.
1089 Tullborg, E.-L., Larson, S.A., Stiberg, J.-P., 1996. Subsidence and uplift of the present
1090 land surface in the southeastern part of the Fennoscandian Shield. GFF 118,
1091 126–128.
1092 Turekian, K.K., Wedepohl, K.H., 1961. Distribution of the Elements in Some Major
1093 Units of the Earth's Crust. Geological Society of America Bulletin 72, 175–
1094 192.
1095 Vine, J.D., Tourtelot, E.B., 1970. Geochemistry of black shale deposits; a summary
1096 report. Economic Geology 65, 253–272.
1097 Wang, F., 2000. Reflectance of vitrinite-like maceral derived from benthic
1098 multicellular algae as organic maturity indicator for pre-Silurian marine
1099 strata, in: AAPG International Conference and Exhibition.
1100 Wignall, P.B., 1994. Black shales, Oxford science publications. Clarendon Press-
1101 Oxford University Press, Oxford-New York.
1102 Wilkin, R.T., Arthur, M.A., 2001. Variations in pyrite texture, sulfur isotope
1103 composition, and iron systematics in the Black Sea: evidence for Late
1104 Pleistocene to Holocene excursions of the O_2-H_2S redox transition.

Geochimica et Cosmochimica Acta 65, 1399–1416.

Yu, B., Dong, H., Widom, E., Chen, J., Lin, C., 2009. Geochemistry of basal Cambrian black shales and cherts from the Northern Tarim Basin, Northwest China: Implications for depositional setting and tectonic history. Journal of Asian Earth Sciences 34, 418–436.

Zhang, Y.-G., Frantz, J.D., 1987. Determination of the homogenization temperatures and densities of supercritical fluids in the system NaCl-KCl-$CaCl_2$-H_2O using synthetic fluid inclusions. Chemical Geology 64, 335–350.

Ziegler, P.A., 1988. Evolution of the Arctic-North Atlantic and the Western Tethys. American Association of Petroleum Geologists, Tulsa, Okla., U.S.A.

Table caption

Table 1 List of samples with corresponding wells and depths

Table 2 Selected metals, carbon, sulfur and phosphorus whole rock concentrations in several Alum Shale samples (Total Organic Carbon TOC, Total Sulfur TS and Total Phosphorus TP are in wt.%. Other elements are in ppm)

Table 3 Rock Eval analyses on several Alum Shale samples. S1 and S2 are in mg HC/g Rock, S3 in mg CO_2/g Rock, T_{max} in °C, TOC in wt.%, HI in mg HC/g TOC and OI mg CO_2/g TOC

Table 4 $\delta^{34}S$ values (in ‰) for different pyrite generations in the Alum Shale Formation

Table 5 Uranium and Rare Earth Element concentrations in apatite-(CaF[OH]) nodules (ppm) from LA-ICP-MS analysis

Table 6 Main features of selected hydrocarbon-bearing inclusions in concretions and fractures. Homogenization temperatures Th are in °C, vapor volume fractions Fv in %, CH4, CO2 and alkane content in mol/kg

Table 7 Peak area and calculated temperatures for Raman spectra on carbonaceous nodules. RA1 and RA2 are two area ratios used to estimate temperature. Carbonaceous matter types (CM) are indicated as PB Cal (Pyrobitumen under calcite), PB (Pyrobitumen) and PV (Pseudo-vitrinite)

Table 8 Composition of U-Ti bearing minerals in Alum Shale determined by EPMA in weight percents of major oxides

Figure captions

Fig. 1 Geological map of the Fennoscandian Shield with main Alum Shale occurrences (modified from Thickpenny, 1984). For a more comprehensive map of Lower Palaeozoic strata in Baltoscandia see Nielsen and Schovsbo, 2015

Fig. 2 a. Metamorphic Alum Shale (Tåsjö) with fractured massive pyrites and calcite in pressure shadows; **b.** Metamorphic Alum Shale (Tåsjö) with fractured pyrite beds and calcite-pyrobitumen fracture fillings (left); **c.** Immature Alum Shale (Västergötland)

Fig. 3 X-Ray diffractograms of immature Alum Shale (Närke) and metamorphic Alum Shale (Tåsjö)

Fig. 4 Average concentrations (As, Co, Cr, Cu, Mo, Ni, Pb, Th, U, V, Zn) in Alum Shale occurrences analyzed for this study (dots for metamorphic samples from Myrviken, Lövstrand and Tåsjö, squares for non metamorphic samples from Närke, Östergötland, Öland, Skåne, Västergötland), compared with reference shales (Marine shales from Turekian and Wedepohl, 1961; Tarim basin black shales from Yu *et al.*, 2009; Ronneburg black shales from Lippmaa *et al.*, 2011; Ohio shale from Lewis *et al.*, 2010)

Fig. 5 a. Carbon-sulfur plot for the Alum Shale Formation. Oxic marine depositional settings and euxinic (anoxic-sulfidic) water column are indicated. Euxinic but Fe-limited sediments would plot along a sub-horizontal trend with an extrapolated positive intercept on the S-axis (Raiswell and Berner, 1985; Leventhal, 1995). **b.** V/(V + Ni) vs. V/Cr crossplot for the Alum Shale Formation. Depositional settings ranges for V/Cr and V/(V + Ni) are from Jones and Manning (1994) and from Hatch and

1162 Leventhal (1992), respectively

1163 **Fig. 6** Uranium-carbon plot (a) and uranium-phosphorus plot (b) for several Alum
1164 Shale occurrences. All values are density-corrected. Artificial maturation residues are
1165 indicated in Fig. 6a

1166 **Fig. 7** Petrographic features of organic matter in the Alum Shale Formation. **a.** UV-
1167 Fluorescent macerals (liptinite) in immature Alum Shale (Östergötland); **b.** UV-
1168 Fluorescent macerals (liptinite) in immature Alum Shale (Närke); **c.** Pseudo-vitrinite
1169 in immature Alum Shale (Närke); **d.** Pyrobitumen in metamorphic Alum Shale
1170 (Myrviken); **e.** Pyrobitumen vein in metamorphic Alum Shale (Tåsjö); **f.** Pyrobitumen
1171 vein (with calcite) in metamorphic Alum Shale (Tåsjö). Bit: pyrobitumen, Cal: calcite,
1172 PV: pseudo-vitrinite, Pyr: pyrite, Qtz:quartz

1173 **Fig. 8** S2 vs. TOC diagram for immature and metamorphic Alum Shale

1174 **Fig. 9** IH vs. Tmax diagram for immature and metamorphic Alum Shale

1175 **Fig. 10** S1 vs. S2 diagram for immature and metamorphic Alum Shale

1176 **Fig. 11** Petrographic features of sedimentary and diagenetic sulfides. **a.** Framboids
1177 and euhedral pyrites in immature Alum Shale (Östergötland); **b.** Detailed view of an
1178 isolated framboid (Västergötland); **c.** Beds of (sub)euhedral pyrites underlining
1179 sedimentary(Tåsjö); **d.** Beds of (sub)euhedral pyrites (Tåsjö); **e.** Massive pyrite with
1180 core of coalescent syn-sedimentary pyrites and large pyrite crystals growing
1181 perpendicularly (Närke); **f.** Large isolated pyrite and deformation of sedimentary
1182 bedding (Närke); **g.** Massive pyrites in heterogeneous porous cement (Östergötland);
1183 **h.** Homogeneous pyrite veins and fracture fillings of euhedral pyrites (Östergötland)

1184 **Fig. 12** As, Cu and Ni content in sulfides from immature and metamorphic Alum

1185 Shale. **a.** Diagenetic pyrite with no particular enrichment in As, Cu and Ni; **b.**
1186 Framboids with high Cu concentration compared to syngenetic euhedral pyrites; **c.**
1187 Synmetamorphic pyrite overgrowth with Ni enrichment and framboids remnants
1188 with high Cu concentration; **d.** Massive diagenetic pyrite with no particular
1189 enrichment and metamorphic overgrowths with Ni-rich pyrite and chalcopyrite
1190 (Ccp)

1191 **Fig. 13** Histogram of $\delta^{34}S$ values of pyrite in the Alum Shale Formation

1192 **Fig. 14 a.** Apatite-(CaF[OH]) nodule surrounded by pyrites in immature Alum Shale
1193 (Östergötland); **b.** Carbonaceous matter veinlet (black) with uranium phospho-
1194 silicates (white) and syn-sedimentary pyrites (light grey) in metamorphic Alum Shale
1195 (Tåsjö); **c.** Porous apatite-(CaF[OH]) nodule surrounded by uranium phospho-
1196 silicates clusters (white) in metamorphic Alum Shale (Tåsjö); **d.** Porous apatite-
1197 (CaF[OH]) nodule surrounded by carbonaceous matter and uranium phospho-
1198 silicates clusters (white) in metamorphic Alum Shale (Tåsjö); **e.** Uranium phospho-
1199 silicates spherulites inside apatite-(CaF[OH]) nodule (Tåsjö); **f.** Apatite-(CaF[OH])
1200 anhedral crystals associated with uranium phospho-silicates and carbonaceous
1201 matter on the edge of a porous apatite-(CaF[OH]) nodule (Tåsjö). Ap: apatite-
1202 (CaF[OH]), C: carbonaceous matter, P-cof: uranium phospho-silicates of various
1203 composition (see text for details), Py: pyrite. Red circles and green circles correspond
1204 to uranium minerals chemical analyses and phosphate nodules LA-ICP/MS
1205 analyses, respectively

1206 **Fig. 15** REE patterns in apatite-(CaF[OH]) nodules from immature and metamorphic
1207 Alum Shale. All spectra are normalized to North American Shale Composite (NASC

1208 REE concentrations after Gromet *et al.*, 1984) and metamorphic shales values are
1209 multiplied by 10 to improve readability
1210 **Fig. 16 a.** Breccia with angular calcite crystals (Öland); **b.** Top view of calcite
1211 concretion (beef) with centimetric crystals (Västergötland); **c.** Hydrocarbon-bearing
1212 inclusions in calcite (Öland); **d.** Aqueous inclusion in calcite (Öland); **e.** UV-
1213 fluorescent oil inclusions (Västergötland); **f.** 3-phase (oil-water-gas) inclusion (Öland)
1214 **Fig. 17** Histograms of homogenization temperatures for fluid inclusions in
1215 concretions (a) and fracture fillings in Ordovician limestones (b)
1216 **Fig. 18** Evolution of vapor volume fraction with homogenization temperature for
1217 various hydrocarbon-bearing inclusions in concretions (blue circles) and fractures
1218 (red squares)
1219 **Fig. 19** Pressure-Temperature diagrams for inclusions in concretions (a) and fractures
1220 (b). Black lines represent isochores and isopleths of petroleum inclusions. Gray bands
1221 represent domain of isochores for aqueous inclusions. Dotted line is determined with
1222 the mode of homogenization temperatures and the mean salinity of aqueous
1223 inclusions. Trapping conditions correspond to intersection of intersection domains in
1224 blue for concretions (A', A, B) and in red for fractures (C, D, and E)
1225 **Fig. 20 a.** Example of Raman spectra obtained on carbonaceous matter in Alum Shale;
1226 **b.** Peak fitting on first order region of Raman spectra using Lorentzian profiles.
1227 Complete dataset in table 3
1228 **Fig. 21** Sulfide modifications in metamorphic Alum Shale. **a.** Cataclased massive
1229 pyrite (Myrviken); **b.** Fractured massive pyrite with pyrite overgrowths and late
1230 calcite fillings (Tåsjö); **c.** Folded bed of framboids and (sub)euhedral pyrites (Tåsjö);

d. Interpenetrative boundaries on euhedral pyrites (Tåsjö); **e.** Framboids in synmetamorphic pyrite overgrowths (Myrviken); **f.** Fractures in pyrites filled with chalcopyrite and sphalerite (Myrviken); **g.** Massive pyrite with chalcopyrite and sphalerite inclusions (Myrviken); **h.** Pyrite-chalcopyrite-sphalerite paragenesis (Myrviken). Ccp: chalcopyrite, Pyr: pyrite, Sph: sphalerite

Fig. 22 a. Brannerite (white) in syn-metamorphic pyrites (Myrviken); **b.** Uraninite (white dots) in syn-metamorphic pyrites surrounded by barite (Tåsjö); **c.** Uranium phospho-silicates in metamorphic Alum Shale (Myrviken); **d.** Altered uraninite core (white) rimmed by uranium phospho-silicates (Tåsjö); **e.** Pyrite rimmed by U-Ti phospho-silicates (Tåsjö); **f.** Brannerite rimmed by U-Ti phospho-silicates (Tåsjö). Brn: brannerite, Brt: barite, Gn: galena, P-cof: uranium phospho-silicates of various composition (see text for details), Py: pyrite, Urn: uraninite. Red circles correspond to uranium mineral chemical analyses

Fig. 23 Ti-Si (a), U-P (b), U+Ca+Y-Si+P (c) and Ca+Y+P-U+Si (d) diagrams for U-Ti-Y minerals in Alum Shale (APFU Atoms Per Formula Unit). Theorical uraninite, (P-)coffinite, brannerite and xenotime are indicated by large black dots. Circles represent Y-poor/Ti-rich minerals (Brannerite group), squares represent Y-poor/Ti-poor minerals (Uraninite group) and diamonds represent Y-rich/Ti-poor minerals (Xenotime group)

Fig. 24 Evolution of $\delta^{34}S$ values in pyrites from sedimentation to metamorphism. Pyrite generations are indicated as Py1 to Py6 in the figure and described in the text

Fig. 25 Uranium-phosphorus plot for the Alum Shale Formation for whole rock (same data as Fig. 6b) and discrete uranium concentrations in phosphate nodules

(frequency of occurrence histogram on the right). The shaded line illustrates the extrapolation at 60 mg.cm^{-3} of phosphorus (average phosphorus content in apatite-(CaF[OH])

Fig. 26 Pressure-Temperature diagram with trapping condition of fluid inclusions and possible evolution pathways: 1) low geothermal gradient pathway (<20°C/km); 2) 20-30°C/km geothermal pathway; 3) low burial

Fig. 27 Schematic scenario proposed to describe the evolution of organic matter, sulfides and uranium in the Alum Shale Formation, from sedimentation to Greenschist metamorphism